New Limit on the Permanent Electric Dipole Moment of ^{129}Xe Using ^{3}He Comagnetometry and SQUID Detection

N. Sachdeva,[1,*] I. Fan,[2] E. Babcock,[3] M. Burghoff,[2] T. E. Chupp,[1] S. Degenkolb,[1,4] P. Fierlinger,[5] S. Haude,[2] E. Kraegeloh,[5,1] W. Kilian,[2] S. Knappe-Grüneberg,[2] F. Kuchler,[5,6] T. Liu,[2] M. Marino,[5] J. Meinel,[5] K. Rolfs,[2] Z. Salhi,[3] A. Schnabel,[2] J. T. Singh,[7] S. Stuiber,[5] W. A. Terrano,[5] L. Trahms,[2] and J. Voigt[2]

[1]*Department of Physics, University of Michigan, Ann Arbor, Michigan 48109, USA*
[2]*Physikalisch-Technische Bundesanstalt (PTB) Berlin, 10587 Berlin, Germany*
[3]*Jülich Center for Neutron Science, 85748 Garching, Germany*
[4]*Institut Laue-Langevin, 38042 Grenoble, France*
[5]*Excellence Cluster Universe and Technische Universität München, 85748 Garching, Germany*
[6]*TRIUMF, Vancouver, British Columbia V6T 2A3, Canada*
[7]*National Superconducting Cyclotron Laboratory and Department of Physics & Astronomy, Michigan State University, East Lansing, Michigan 48824, USA*

(Received 8 February 2019; published 4 October 2019)

We report results of a new technique to measure the electric dipole moment of ^{129}Xe with ^{3}He comagnetometry. Both species are polarized using spin-exchange optical pumping, transferred to a measurement cell, and transported into a magnetically shielded room, where SQUID magnetometers detect free precession in applied electric and magnetic fields. The result from a one week measurement campaign in 2017 and a 2.5 week campaign in 2018, combined with detailed study of systematic effects, is $d_A(^{129}\mathrm{Xe}) = (1.4 \pm 6.6_{\mathrm{stat}} \pm 2.0_{\mathrm{syst}}) \times 10^{-28}$ e cm. This corresponds to an upper limit of $|d_A(^{129}\mathrm{Xe})| < 1.4 \times 10^{-27}$ e cm (95% C.L.), a factor of 5 more sensitive than the limit set in 2001.

DOI: 10.1103/PhysRevLett.123.143003

Searches for permanent electric dipole moments (EDMs) are a powerful way to investigate beyond-standard-model (BSM) physics. An EDM is a charge asymmetry along the total angular momentum axis of a particle or system and is odd under both parity reversal (P) and time reversal (T). Assuming CPT conservation (C is charge conjugation), an EDM is a direct signal of CP violation (CPV), a condition required to generate the observed baryon asymmetry of the universe [1]. The standard model (SM) incorporates CPV through the phase in the CKM matrix and the QCD parameter $\bar{\theta}$. However, the SM alone is insufficient to explain the size of the baryon asymmetry [2]. BSM scenarios that generate the observed baryon asymmetry [3] generally also provide for EDMs larger than the SM estimate, which for ^{129}Xe is $|d_A(^{129}\mathrm{Xe})^{\mathrm{SM}}| \approx 5 \times 10^{-35}$ e cm [4].

EDM measurements have provided constraints on how BSM CPV can enter low-energy physics [4]. Diamagnetic systems such as ^{129}Xe and ^{199}Hg are particularly sensitive to CPV nucleon-nucleon interactions that induce a nuclear Schiff moment and CPV semileptonic couplings [5]. While the most precise atomic EDM measurement is from ^{199}Hg [6], there are theoretical challenges to constraining hadronic CPV parameters from ^{199}Hg alone, and improved sensitivity to the ^{129}Xe EDM would tighten these constraints [5,7]. Additionally, recent work has shown that contributions from light-axion-induced CPV are significantly stronger for ^{129}Xe than for ^{199}Hg [8]. ^{129}Xe also may be used as a comagnetometer in future neutron EDM experiments [9,10].

The first ^{129}Xe EDM measurement by Vold *et al.* monitored ^{129}Xe Larmor precession frequency as a function of applied electric field [11]. Rosenberry *et al.* [12] used a two-species maser with a ^{3}He comagnetometer. A number of ^{129}Xe EDM efforts to improve on this limit have followed, including an active maser technique [13], and an experiment with polarized liquid xenon [14]. Recently the result of an experiment using ^{3}He and SQUID detection, but with a different approach to EDM extraction and systematic effects, was reported [15]. The early developments of our approach are described in Ref. [16].

For a system with total angular momentum $\vec{F}$, EDM $d\vec{F}/F$, and magnetic moment $\mu\vec{F}/F$, the Hamiltonian is $H = -(\mu\vec{F}\cdot\vec{B} + d\vec{F}\cdot\vec{E})/F$. This results in an energy splitting dependent on $\vec{E}\cdot\hat{B}$ and a corresponding frequency shift $\omega_d = \pm d|E|/(\hbar F)$ between states with $|\Delta m_F| = 1$. Changes of $\vec{B}$ due to drifts and extraneous magnetic fields lead to frequency shifts that are mitigated by comagnetometry—simultaneous measurement with a colocated species. The ^{129}Xe-^{3}He comagnetometer system is favorable because both can be simultaneously polarized by spin-exchange optical pumping (SEOP) [17], have long spin relaxation times enabling precision frequency measurements, and ^{3}He, with

$27\times$ lower nuclear charge Z, is much less sensitive to *CP* violation [18].

We present the combined results of two HeXeEDM campaigns in 2017 and 2018 at the BMSR-2 (Berlin Magnetically Shielded Room) facility at Physikalisch-Technische Bundesanstalt (PTB) Berlin. The layout of the experiment is shown in Fig. 1. Free precession of ^{129}Xe and ^{3}He was measured with low-noise superconducting quantum interference devices (SQUIDs). The BMSR-2 provided a passive shielding factor of more than 10^8 above 6 Hz [19]. A 1.6 m diameter set of Helmholtz coils generated the static magnetic field (B_0) of 2.6–3.0 μT along the y axis in 2017 and x axis in 2018. In a separate setup similar to that described in Ref. [20], for the 2017 (2018) campaign, the gas mixture of 18% (15%) isotopically enriched xenon (90% ^{129}Xe), 73%(75%) ^{3}He, and 9%(15%) N_2 was polarized by SEOP in a refillable optical pumping cell (OPC). Simultaneous polarization of ^{129}Xe-^{3}He mixtures compromise both polarizations because the optimum conditions are very different for the two species. Typically, we achieved 5–15% polarization for ^{129}Xe and 0.1–0.2% (2017) or 0.5–1.4% (2018) polarization for ^{3}He depending on the total pressure in the OPC. Data were taken with three EDM cells with 30 mm diameter, 2 mm thickness, p type (Boron) doped 1–10 Ω cm silicon electrodes diffusion bonded to borosilicate glass cylinders [21]. One cell (PP1) had a length of 18.5 mm and an inner diameter of 20.5 mm; PP2 and PP3 both had a length of 21.8 mm and an inner diameter of 20.4 mm. PP1 and PP2 were used in 2017; all three cells were used in 2018. Before each filling, the EDM cell was degaussed using a commercial bulk degausser [22]. The polarized gas was expanded from the OPC into an evacuated EDM cell. Each time the OPC was refilled, the polarized gas was used for two EDM cell fillings: the first had higher pressure ($\sim$1 bar) and the second had lower pressure ($\sim$0.5 bar). Toward the end of the 2018 campaign, we shifted to using only higher pressures in a scheme that prioritized ^{129}Xe polarization, resulting in improved SNR and a reduction of the comagnetometer drift discussed below. After the EDM cell was filled, it was transported to the magnetically shielded room in a battery-powered 400 μT shielded solenoid and positioned under the SQUID Dewar. For the 2017 campaign, we applied a time-dependent magnetic field along the x axis with resonant frequency components and amplitudes tuned to effect a $\pi/2$ pulse for both species. For 2018, the magnetic field was diabatically switched within 0.5 ms from $\hat{y}$ to $\hat{x}$. For both campaigns, data were acquired from the Z_1 SQUID, which was located 50 mm (2017) and 36 mm (2018) above the center of the EDM cell. A grounded silicon wafer was placed between the EDM cell and Dewar as indicated in Fig. 1 to protect the SQUIDs from HV discharges.

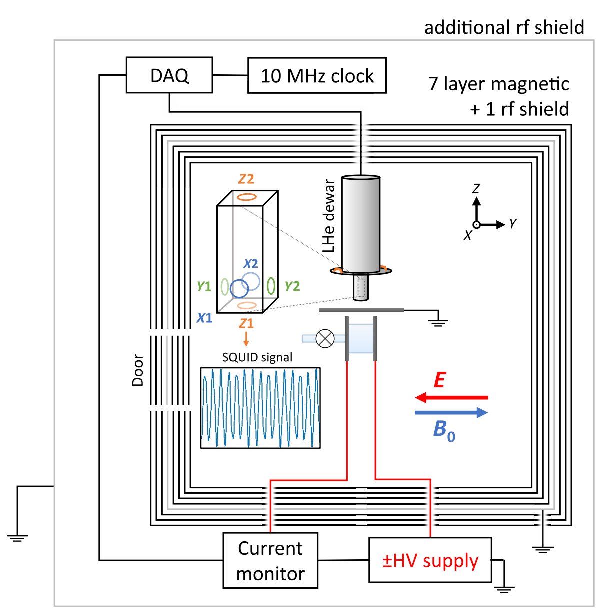

FIG. 1. Schematic of the HeXeEDM apparatus at PTB. The electric field $\vec{E}$ indicated corresponded to +HV and the magnetic field is shown along $+\hat{y}$ for 2017. In 2018, the electric and magnetic fields were along $\hat{x}$. The inset shows a typical raw SQUID signal for 1/2 second of data; the frequencies were 30.8 Hz (35.2 Hz) for ^{129}Xe and 84.8 Hz (97.0 Hz) for ^{3}He in 2017 (2018). Not to scale.

The data-acquisition sample rate of 915.5245 Hz was derived from the 10 MHz output of an external clock [23]. The initial amplitudes of the precession signals were about 30 pT and 5 pT for ^{129}Xe and ^{3}He, respectively, in 2017, and 20–70 pT and 17–50 pT in 2018. The noise measured by the SQUID system was 6 fT/$\sqrt{\mathrm{Hz}}$. The free precession decay time T_2^* did not differ significantly between the two campaigns and was in the range of 3000–10 000 s for ^{129}Xe and 4000–10 000 s for ^{3}He. The precession was measured typically for about 15 000 s in 2017 and 25 000–45 000 seconds in 2018, which we define as a *run*. During each run, a pattern of HV polarity changes modulated the EDM signal. A pattern with changes in equal length intervals defines a *subrun*. In 2018, there were 1–4 subruns within a run with different segment lengths; in 2017, there was only one subrun per run.

HV of $\pm$6–9 kV was applied to one electrode with the other electrode connected via the current monitor to ground potential. In 2017, the average electric fields were 3.2 kV/cm and 2.7 kV/cm across cells PP1 and PP2, respectively. In 2018, the electric fields ranged from 2.7 kV/cm to 4.8 kV/cm. The voltage was chosen to be below the observed breakdown voltage.

During each subrun, the HV polarity was positive (+), negative (−), or zero for equal intervals called segments. Segments with zero HV were inserted at the beginning and end of each set of 16 segments within a subrun [24]. The rate of change of HV between segments (HV ramp) was set to either 1 or 2 kV/s in 2017 and 0.5 or 1 kV/s in 2018.

Segment lengths of 400 or 800 seconds for 2017 and between 100 to 600 seconds for 2018 were chosen based on the Allan deviation minimum from studies before taking EDM data. During analysis, an F test was used to check for comagnetometer drift within segments. In 2017, five segments out of a total of 539 segments were shortened accordingly due to comagnetometer drift and an additional eight were shortened because of HV or SQUID problems. For 2018, four runs were removed: three due to HV spark and SQUID irregularities and one due to a large magnetic field shift halfway through the run.

The raw time-domain SQUID data were processed by first removing the dc offset and baseline drift with a high-pass filter. Filtered data were divided into nonoverlapping blocks of length $\tau = 20$ seconds, short enough that amplitude decay and frequency drift were negligible. Data for each block were fit using a separable nonlinear least-squares method [25] to a six-parameter model to determine the amplitude, frequency, and phase $\Phi^m_{\mathrm{Xe/He}}$ for block m for each species (see the Supplement Material [26]). An independent analysis was performed using an alternative approach, which did not use the high-pass filter but added an offset and linear drift term to the fit function as described in [27], and produced consistent results.

Magnetic field drifts were compensated by the comagnetometer corrected phases $\Phi^m_{\mathrm{co}} = \Phi^m_{\mathrm{Xe}} - R\Phi^m_{\mathrm{He}}$, where $R = 1/2.7540816$ is the nominal ratio of the shielded gyromagnetic ratios of ^{129}Xe and ^{3}He [28]. For each HV segment, the comagnetometer frequency ω_{co} and uncertainty were determined from the slope of a linear fit to Φ^m_{co} as a function of time. The frequency uncertainties were consistent with the minimum expected uncertainties based on the signal amplitude, noise, and segment duration [24,29,30]. Segment frequencies were blinded by adding or subtracting, depending on the sign of $\vec{E}\cdot\hat{B}$, an unknown offset derived from a previously computer-generated pseudorandom number such that $|\omega^{2017}_{\mathrm{blind}}|/(2\pi) \leq 50$ nHz or $|d^{2018}_{\mathrm{blind}}| \leq 5\times 10^{-27}$ e cm. The blinding offsets were saved separately from the data in a binary format. After all cuts and systematic corrections were determined, the blinding offset was set to zero to produce the set of HV segment frequencies for the final unblinded EDM analysis.

The EDM frequency was determined from an average of four consecutive segment frequencies with HV $(+--+)$ or $(-++-)$ to compensate for linear drifts of the comagnetometer frequencies, typically a few μHz over the course of a run. The EDM for each subrun was determined from the weighted average of the four-segment EDM frequencies within the subrun.

Systematic effects include the uncertainties of experimental parameters as well as false-EDM signals that may arise from the nonideal response of the comagnetometer. The comagnetometer frequency ω_{co} can be described by the following four dominant terms plus the EDM contribution $\omega_d \equiv \omega_{d_{\mathrm{Xe}}} - R\omega_{d_{\mathrm{He}}}$:

$$\omega_{\mathrm{co}} \approx \omega_d - \gamma'_{\mathrm{He}}\Delta R B + (1-R)\vec{\Omega}\cdot\hat{B} + \gamma'_{\mathrm{Xe}}(\Delta B^{\mathrm{dif}}_{\mathrm{Xe}} - \Delta B^{\mathrm{dif}}_{\mathrm{He}}) + (\omega^{sd}_{\mathrm{Xe}} - R\omega^{sd}_{\mathrm{He}}). \quad (1)$$

Here, $\gamma'_{\mathrm{He/Xe}}$ are the shielded gyromagnetic ratios; ΔR is a correction to R that changed from run to run due mostly to pressure dependence of the chemical shifts; $\vec{B}$ is the average magnetic field within the cell with contributions from the applied magnetic field $\vec{B}_0$, the ambient magnetic field of the room, and any nearby magnetized materials; $\vec{\Omega}$ is the angular frequency of the Earth's rotation; and $\Delta B^{\mathrm{dif}}_{\mathrm{Xe/He}}$ represents the difference of the volume averaged magnetic field and the field averaged by the atoms of each species as they diffuse through the cell. In the presence of second- and higher-order gradients, this average is different for the two species [31].

The second through fourth terms in Eq. (1) indicate the residual sensitivity of ω_{co} to the magnitude, direction, and gradients of the magnetic field, and any correlation of these with the HV may cause a false-EDM signal. Such correlations are expected from possible leakage currents, magnetization induced by charging currents that flow when the HV is changed, and motion of the measurement cell due to electrostatic forces. Our approach to estimating false-EDM signals is based on auxiliary measurements of the dependence of ω_{co} on amplified leakage and charging currents, gradients, and cell motion, which are scaled to the HV correlations of these parameters monitored during the experiment. The last term in Eq. (1) reflects time-dependent, species-dependent shifts, predominantly due to effects of residual longitudinal magnetization that dominate the comagnetometer drift [32,33]. Equation (1) does not include $\vec{E}\times\vec{v}$ effects, which are negligible.

Systematic effects, including false EDM contributions and their uncertainties for both campaigns, are listed in Table I. During each campaign, an auxiliary measurement of the comagnetometer response to a leakage current was simulated by a single turn of wire wrapped around the cell and scaled by the observed maximum leakage current of 97 pA in 2017 and 73 pA in 2018. Since the leakage current followed an unknown path that could increase or decrease B, we consider this an upper limit on the magnitude of a false EDM. During each HV ramp, the charging current might have induced magnetization of materials in or near the cell, correlated with the change of HV. The comagnetometer response to charging currents of ± 10 and ± 20 μA was measured and scaled by the maximum charging current observed for the EDM data.

The electric force between the cell electrodes and the grounded safety electrode might have caused cell movement when the electric field was changed, affecting the magnetic fields and gradients across the cell. The effect of cell rotation on the comagnetometer frequency was measured by rotating the cell $\pm 5°$ around the z axis.

TABLE I. Summary of EDM results and systematic effects discussed in the text.

	2017 (e cm)	2018 (e cm)
EDM	7.2×10^{-28}	0.9×10^{-28}
Statistical error	23.5×10^{-28}	6.8×10^{-28}
Systematic Source		
Leakage current	1.2×10^{-28}	4.5×10^{-31}
Charging currents	1.7×10^{-29}	1.2×10^{-29}
Cell motion (rotation)	4.2×10^{-29}	4.0×10^{-29}
Cell motion (translation)	2.6×10^{-28}	1.9×10^{-28}
Comagnetometer drift	2.6×10^{-28}	4.0×10^{-29}
$\vert\vec{E}\vert^2$ effects	1.2×10^{-29}	2.2×10^{-30}
$\vert\vec{E}\vert$ uncertainty	2.6×10^{-29}	9.4×10^{-30}
Geometric phase	$\leq 2 \times 10^{-31}$	$\leq 2 \times 10^{-31}$
Total Systematic Error	3.9×10^{-28}	2.0×10^{-28}

HV-correlated cell rotation was investigated by measuring the motion of a laser beam spot reflected from the cell electrode with a lever arm of 1.5m and estimated to be less than 33 μrad. HV-correlated translation of the cell in a nonuniform magnetic field might produce a false EDM because of the change of B in the cell [second term in Eq. (1)] or through a change of the higher-order gradients [fourth term in Eq. (1)]. The fourth term in Eq. (1) is dominant and was isolated with an auxiliary measurement of $\partial\omega_{\mathrm{co}}/\partial\omega_{\mathrm{He}}$ for a loop mounted on a cell electrode combined with $\delta\omega_{\mathrm{He}}$. This provided an upper limit on any HV correlated effect, including cell translation, due to a source of magnetic field gradient outside the cell, provided the size of the source was smaller than its distance from the cell [26].

Uncompensated drift of ω_{co} would appear as a false EDM due to the frequency shift between segments with opposite $\vec{E} \cdot \hat{B}$. The time dependence of the comagnetometer frequency drifts for all subruns could be accurately parametrized by polynomials of the first through fifth order depending on the size of the drift and the signal-to-noise ratio. Offsets and linear drifts were compensated by the four-segment HV reversal pattern, while drifts characterized by second- and third-order time dependence would be removed by the 8- and 16-segment HV patterns, respectively. Because the linear time dependence is dominant, we have chosen to extract the EDM using four-segment measurements ($+--+$ or $-++-$) and to apply a correction for quadratic and higher order time dependence. The correction was estimated from the weighted polynomial coefficients of the fits to the comagnetometer frequency drift for each subrun. The highest polynomial order needed to accurately parametrize the drift for each subrun was determined by applying an F test. A threshold of $F_{\min} = 0.6$ was chosen for both data sets. The uncertainty on this correction is a statistical error based on the polynomial fits to the segment frequencies for each run, but is compiled as a systematic error in Table I to emphasize that it may give rise to a false EDM. For the 2018 analysis, we applied the comagnetometer drift correction to the EDM for each subrun and included correlations between coefficients. Applying this method to the 2017 data resulted in a shift of the central value reported in [24,34] by approximately the estimated systematic uncertainty.

$|\vec{E}|^2$ effects included any shift that depended on the magnitude of the applied electric field, for example, chemical shifts or HV-induced noise detected by the SQUID. Segments with $E = 0$ and the different E enabled studies of the correlation of comagnetometer frequency with $|E|$ and $|\vec{E}|^2$. The modeling of the average electric field in the cell in the presence of the protection electrode contributed an uncertainty of $0.1 d_A$. The combination of $\vec{E} \times \vec{v}$ effects coupled with magnetic field gradients could produce a false EDM, often referred to as a geometric phase. In gases at the densities used for these experiments, the time between collisions is small compared to the spin-precession period, which mitigates the coherent buildup of phase linear in the electric field. The formalism of Ref. [35] was used to estimate an upper limit.

In 2017 and 2018, respectively, there were a total of 16 runs and subruns and 25 runs (64 subruns) measured under different conditions including measurement cell, gas pressure, $\vec{B}_0$ direction, HV ramp rate, starting HV polarity, and HV segment length. Figure 2 shows a comparison of sorting all EDM measurements into groups based on these variables, including EDM uncertainty σ_{d_i}, and Fig. 3 shows the EDM measurements per run that had different cells, cell pressures, and orientations of $\vec{B}_0$ for 2017 and 2018. We also investigated correlations between the extracted EDM

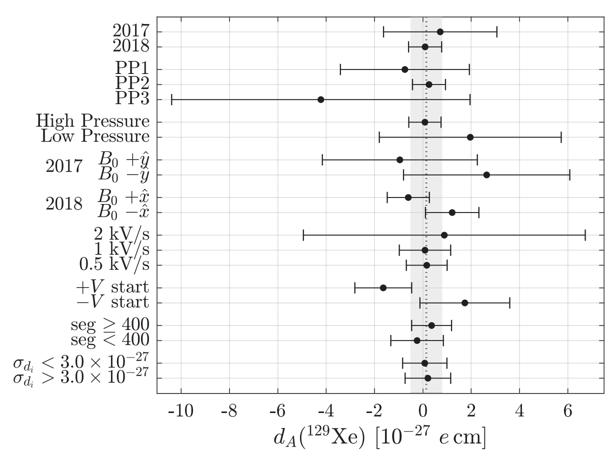

FIG. 2. Comparison of EDM measurements for both the 2017 and 2018 campaigns grouped by cell, cell pressure, $\hat{B}_0$ direction, HV ramp rate, HV start polarity, HV segment length, and EDM uncertainty $\sigma_{d_i} < 3.00 \times 10^{-27}$ e cm (five subruns) or $\sigma_{d_i} > 3.00 \times 10^{-27}$ e cm (75 subruns). The shaded area shows the result given in Eq. (2).

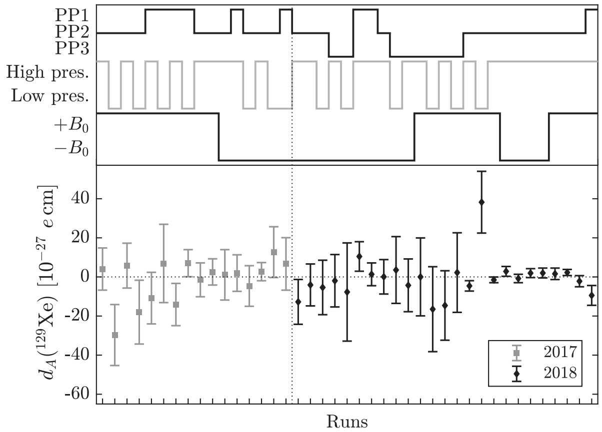

FIG. 3. All drift-corrected EDM measurements by run indicating the cell used, cell pressure, and the magnetic field direction. During the 2018 run, an adjusted polarization routine resulted in a reduction of the comagnetometer drift allowing for longer segments and increased SNR. Therefore, runs from the last week of data collection had improved statistical sensitivity.

and other parameters including T_2^* and comagnetometer drift rate [26].

The comagnetometer-drift corrected results for 2017 and 2018 were confirmed with two independent analyses and are presented in Table I. The combined result is

$$d_A(^{129}\mathrm{Xe}) = [1.4 \pm 6.6(\mathrm{stat})] \times 10^{-28}\ e\,\mathrm{cm}. \quad (2)$$

The statistical error is the uncertainty of the weighted average of the uncorrected measurements, and $\chi^2 = 68$ for 79 degrees of freedom Combined with the systematic error from Table I, we find $|d_A(^{129}\mathrm{Xe})| \leq 1.4 \times 10^{-27}\ e\,\mathrm{cm}$ (95% C.L.). This is a factor of 5 improvement in sensitivity over the previous limit of $|d_A(^{129}\mathrm{Xe})| \leq 6.6 \times 10^{-27}\ e\,\mathrm{cm}$ (95% C.L.) [12]. Bootstrapping [36] the unblinded 2017 and 2018 subrun data to estimate the error on the mean resulted in an estimate of $7.4 \times 10^{-28}\ e\,\mathrm{cm}$.

Further improvement to the polarization, SQUID Dewar noise, measurement time, and increased electric field should result in an order of magnitude or more in ^{129}Xe EDM sensitivity. The comagnetometer drift can be reduced with a more precise $\pi/2$ flip, tuning the ratio of $^{129}\mathrm{Xe}/^{3}\mathrm{He}$ polarizations, which was shown to be effective at the end of the 2018 campaign, and an optimized EDM cell shape [33]. Precise cell motion measurements are also essential.

This improved limit improves constraints on the low-energy CPV parameters developed in Refs. [4,5], in particular lowering the limits on $\bar{g}_\pi^{0,1}$ and $\bar{\theta}$ by factors of two and C_T by a factor of about 5 [37]; it can also be used to constrain the QCD axion contribution to EDMs by a factor of about five compared to that reported in [8].

We wish to thank Patrick Pistel and Roy Wentz for excellence and innovation in glass blowing and cell construction. This work was supported in part by NSF Grant No. PHY-1506021, DOE Grant No. DE-FG0204ER41331, Michigan State University, by Deutsche Forschungsgemeinschaft Grants No. TR408/12 and No. FA1456/1-1, and The Cluster of Excellence "Origin and Structure of the Universe." W. T. acknowledges the support of a Humboldt Stiftung Fellowship.

*sachd@umich.edu

[1] A. Sakharov, Usp. Fiz. Nauk **161**, 61 (1991) [Sov. Phys. Usp. **34**, 392 (1991)].
[2] M. Dine and A. Kusenko, Rev. Mod. Phys. **76**, 1 (2003).
[3] D. E. Morrissey and M. J. Ramsey-Musolf, New J. Phys. **14**, 125003 (2012).
[4] T. E. Chupp, P. Fierlinger, M. J. Ramsey-Musolf, and J. T. Singh, Rev. Mod. Phys. **91**, 015001 (2019).
[5] T. Chupp and M. Ramsey-Musolf, Phys. Rev. C **91**, 035502 (2015).
[6] B. Graner, Y. Chen, E. G. Lindahl, and B. R. Heckel, Phys. Rev. Lett. **116**, 161601 (2016).
[7] N. Yamanaka, B. K. Sahoo, N. Yoshinaga, T. Sato, K. Asahi, and B. P. Das, Eur. Phys. J. A **53**, 54 (2017).
[8] V. A. Dzuba, V. V. Flambaum, I. B. Samsonov, and Y. V. Stadnik, Phys. Rev. D **98**, 035048 (2018).
[9] S. Degenkolb, A. Leanhardt, and T. Chupp, in *43rd Annual Meeting of the APS Division of Atomic, Molecular and Optical Physics* (2012), Vol. 57, http://meetings.aps.org/link/BAPS.2012.DAMOP.J6.9
[10] Y. Masuda, K. Asahi, K. Hatanaka, S.-C. Jeong, S. Kawasaki, R. Matsumiya, K. Matsuta, M. Mihara, and Y. Watanabe, Phys. Lett. A **376**, 1347 (2012).
[11] T. G. Vold, F. J. Raab, B. Heckel, and E. N. Fortson, Phys. Rev. Lett. **52**, 2229 (1984).
[12] M. A. Rosenberry and T. E. Chupp, Phys. Rev. Lett. **86**, 22 (2001).
[13] T. Inoue *et al.*, Eur. Phys. J. D **70**, 129 (2016).
[14] M. P. Ledbetter, S. Pustelny, D. Budker, M. V. Romalis, J. W. Blanchard, and A. Pines, Phys. Rev. Lett. **108**, 243001 (2012).
[15] F. Allmendinger, I. Engin, W. Heil, S. Karpuk, H.-J. Krause, B. Niederländer, A. Offenhäusser, M. Repetto, U. Schmidt, and S. Zimmer, Phys. Rev. A **100**, 022505 (2019).
[16] F. Kuchler *et al.*, Hyperfine Interact. **237**, 95 (2016).
[17] T. E. Chupp, E. R. Oteiza, J. M. Richardson, and T. R. White, Phys. Rev. A **38**, 3998 (1988).
[18] V. V. Flambaum and J. S. M. Ginges, Phys. Rev. A **65**, 032113 (2002).
[19] J. Bork, H.-D. Hahlbohm, R. Klein, and A. Schnabel, *Proceedings of 13th International Conference on Biomagnetism (Biomag 2002)* (VDE Verlag GMBH, Berlin, 2002), p. 970.
[20] E. S. Korchak, W. Kilian, and L. Mitschang, Appl. Magn. Reson. **44**, 65 (2013).
[21] P. Pistel (private communication).
[22] SV91 m from Verity Systems, Placerville Ca., USA.
[23] BVA8607 from Oscilloquartz S. A., CH-2002 Neuchâtel 2, Switzerland.

[24] N. Sachdeva, A measurement of the permanent electric dipole moment of ^{129}Xe, Ph.D. thesis, University of Michigan, 2019.
[25] G. Golub and V. Pereyra, Inverse Probl. **19**, R1 (2003).
[26] See Supplemental Material at http://link.aps.org/supplemental/10.1103/PhysRevLett.123.143003 for details on the frequency extraction, approach to comagnetometer systematics, and comagnetometer drift correction.
[27] C. Gemmel, W. Heil, S. Karpuk, K. Lenz, Y. Sobolev, K. Tullney, M. Burghoff, W. Kilian, S. Knappe-Grüneberg, W. Müller, A. Schnabel, F. Seifert, L. Trahms, and U. Schmidt, Phys. Rev. D **82**, 111901(R) (2010).
[28] I. Fan *et al.*, J. Phys. Conf. Ser. **723**, 012045 (2016).
[29] T. E. Chupp, R. J. Hoare, R. L. Walsworth, and B. Wu, Phys. Rev. Lett. **72**, 2363 (1994).
[30] Y. Chibane, S. K. Lamoreaux, J. M. Pendlebury, and K. F. Smith, Meas. Sci. Technol. **6**, 1671 (1995).
[31] D. Sheng, A. Kabcenell, and M. V. Romalis, Phys. Rev. Lett. **113**, 163002 (2014).
[32] W. A. Terrano, J. Meinel, N. Sachdeva, T. E. Chupp, S. Degenkolb, P. Fierlinger, F. Kuchler, and J. T. Singh, Phys. Rev. A **100**, 012502 (2019).
[33] M. E. Limes, N. Dural, M. V. Romalis, E. L. Foley, T. W. Kornack, A. Nelson, L. R. Grisham, and J. Vaara, Phys. Rev. A **100**, 010501(R) (2019).
[34] N. Sachdeva *et al.*, arXiv:1902.02864.
[35] G. Pignol, M. Guigue, A. Petukhov, and R. Golub, Phys. Rev. A **92**, 053407 (2015).
[36] B. Efron, *The Jackknife, the Bootstrap and Other Resampling Plans* (Society for Industrial and Applied Mathematics, Philadelphia, 1982).
[37] T. Chupp, M. Ramsey-Musolf, and N. Sachdeva (to be published).

Supplemental material for: New Limit on the Permanent Electric Dipole Moment of ^{129}Xe Using ^{3}He Comagnetometry and SQUID Detection

N. Sachdeva,[1,*] I. Fan,[2] E. Babcock,[3] M. Burghoff,[2] T. E. Chupp,[1] S. Degenkolb,[1,4] P. Fierlinger,[5] S. Haude,[2] E. Kraegeloh,[5,1] W. Kilian,[2] S. Knappe-Grüneberg,[2] F. Kuchler,[5,6] T. Liu,[2] M. Marino,[5] J. Meinel,[5] K. Rolfs,[2] Z. Salhi,[3] A. Schnabel,[2] J. T. Singh,[7] S. Stuiber,[5] W. A. Terrano,[5] L. Trahms,[2] and J. Voigt[2]

[1]*Department of Physics, University of Michigan, Ann Arbor, Michigan 48109, USA*
[2]*Physikalisch-Technische Bundesanstalt (PTB) Berlin, 10587 Berlin, Germany*
[3]*Jülich Center for Neutron Science, 85748 Garching, Germany*
[4]*Institut Laue-Langevin, 38042 Grenoble, France*
[5]*Excellence Cluster Universe and Technische Universität München, 85748 Garching, Germany*
[6]*TRIUMF, Vancouver, British Columbia V6T 2A3, Canada*
[7]*National Superconducting Cyclotron Laboratory and Department of Physics & Astronomy, Michigan State University, East Lansing, Michigan 48824, USA*
(Dated: September 26, 2019)

FREQUENCY EXTRACTION

The EDM was determined from the comagnetometer frequency following the procedure described in this section. The top plot of Fig. 1 shows the raw SQUID data from a run in 2017 and Fig. 3 shows the same for a run in 2018. The offset from the SQUID working point and the baseline drift, which was largely due to magnetic field drift, were both removed with a finite impulse response (FIR) high-pass filter. An FIR filter has the advantage of having an exactly linear phase response, and the resulting group delay was easily corrected. The specific filter used was an equiripple linear-phase FIR filter with a passband frequency of 5 Hz and a stopband-edge frequency of 0.5 Hz. Also shown in Figs. 1 and 3 is the separation of data into segments defined by a single high-voltage (HV) state. HV segments were typically 400 or 800 seconds long for 2017 data and 100–600 seconds long for 2018 data. Data during the HV ramps between segments were excluded. Each segment was divided into non-overlapping blocks of duration $\tau = 20$ seconds, chosen to be short enough that magnetic field drift and amplitude decay were negligible and long enough to separate the ^{129}Xe and ^{3}He frequencies. The data were fit to the following model:

$$S(t) = a_{\mathrm{Xe}} \sin \omega'_{\mathrm{Xe}} t + b_{\mathrm{Xe}} \cos \omega'_{\mathrm{Xe}} t + a_{\mathrm{He}} \sin \omega'_{\mathrm{He}} t + b_{\mathrm{He}} \cos \omega'_{\mathrm{He}} t. \tag{1}$$

The fits were performed using the separable non-linear least squares method described in [1] using Levenberg-Marquardt least-squares minimization over a fixed time interval $[-\tau/2, \tau/2]$. The phase for each species at the center of each block, labeled by index m, was $\phi^m_{\mathrm{Xe/He}} = \arctan\left(b^m_{\mathrm{Xe/He}}/a^m_{\mathrm{Xe/He}}\right)$. A two-argument four-quadrant inverse tangent function was used to return a phase in the domain $[-\pi, \pi]$. Extracting the continuous phase evolution required "unwrapping" the phase, that is adding or subtracting 2π each time the inverse-tangent shifted non-continuously. The unwrapped phase was $\Phi^m_{\mathrm{Xe/He}} = \phi^m_{\mathrm{Xe/He}} + 2\pi N_m$, where N_m is the integer number of cycles prior to the beginning of the segment. The phase at each time $t_m = m\tau$ was determined using

$$\Phi^m_{\mathrm{Xe/He}} = \phi^m_{\mathrm{Xe/He}} + \left\{ \Phi^{m-1}_{\mathrm{Xe/He}} + \omega^{m-1}_{\mathrm{Xe/He}}\tau - \left(\Phi^{m-1}_{\mathrm{Xe/He}} + \omega^{m-1}_{\mathrm{Xe/He}}\tau \right) \mathrm{mod}(2\pi) \right\}. \tag{2}$$

The term in brackets is $2\pi N_m$. The uncertainty of $\Phi^m_{\mathrm{Xe/He}}$ was estimated from standard gaussian error propagation using the parameter uncertainties of $a^m_{\mathrm{Xe/He}}$ and $b^m_{\mathrm{Xe/He}}$, obtained from computation of the covariance matrix of the fit to Eq. 1, which was scaled by the mean-squared-error of the residuals from the fit. Frequencies were determined by a linear least-squares fit of the phase as a function of time over each segment. To get the comagnetometer frequency, the correction was applied to the ^{129}Xe phase using $\Phi_{\mathrm{Xe,co}} = \Phi_{\mathrm{Xe}} - R\Phi_{\mathrm{He}}$, where $R = 1/r$ and $r \equiv 2.7540816$ is the number used in the analysis which is the nominal ratio of the ^{3}He and ^{129}Xe shielded gyromagnetic ratios [2].

COMAGNETOMETER SYSTEMATICS

Ideally, a comagnetometer EDM measurement uses two species with identical responses to magnetic perturbations and very different sensitivities to CPV effects. We have chosen ^{129}Xe and ^{3}He, two $F = 1/2$ atoms. Note that both ^{129}Xe and ^{3}He have negative magnetic moments, *i.e.* the magnetic moment is opposite the total angular momentum

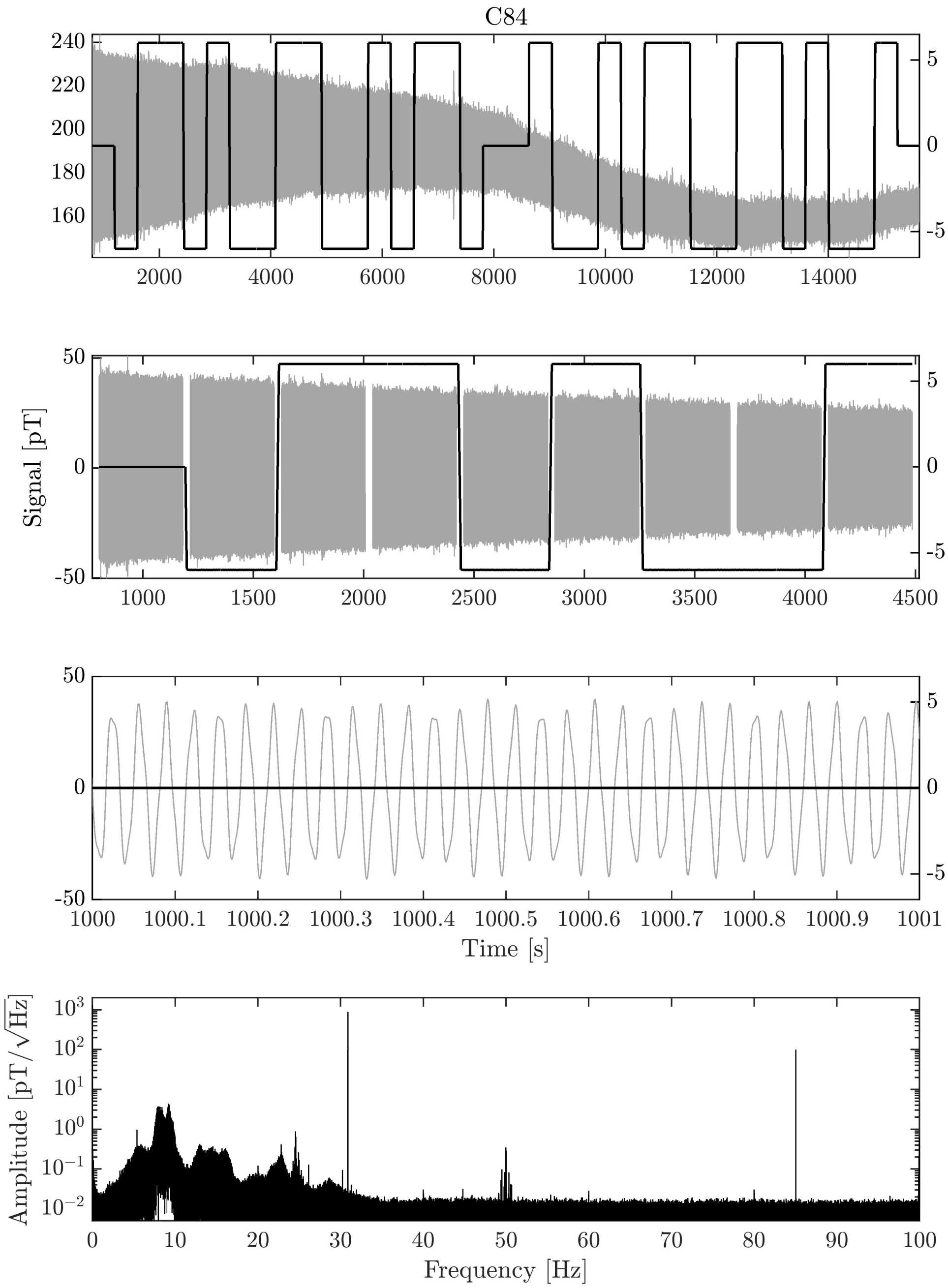

FIG. 1. Top: Unfiltered data (left axis, gray) and the HV pattern (right axis, black) for a single run in 2017. SQUID offset and baseline drift is visible. Middle top: High-pass filtered data (left axis, gray) that has been cut according to the HV states (right axis, gray). Middle bottom: One second of high-pass filtered data shows the two frequencies (30 Hz for ^{129}Xe and 85 Hz for ^{3}He) superposed. Bottom: FFT of unfiltered signal. The bandwidth is ~ 0.4 times the sampling rate of 915.5 Hz.

$\vec{F}$; therefore, for positive $\vec{d}$ (parallel to $\vec{F}$), the precession frequency will decrease when $\vec{E}$ is parallel to $\hat{B}$ ($\vec{E}\cdot\hat{B} > 0$). Thus, an EDM contributes a frequency shift to each species given by

$$\omega_{d_{\mathrm{Xe}}} = -\frac{2d_A(^{129}\mathrm{Xe})}{\hbar}\vec{E}\cdot\hat{B} \qquad \omega_{d_{\mathrm{He}}} = -\frac{2d_A(^{3}\mathrm{He})}{\hbar}\vec{E}\cdot\hat{B}, \tag{3}$$

where the ^{3}He EDM is strongly suppressed because diamagnetic atoms' sensitivity to CPV is approximately proportional to Z^2 [3].

Potential systematic effects, *i.e.* false-EDM signals, arise because the two species have different responses to the magnetic field environment due to chemical shifts, diffusion in magnetic field gradients, and species-dependent self and cross-species interactions. Additionally, the apparatus that measures the spin precession rotates with the Earth, adding an offset to the precession frequencies. Taking these into account, the two species' precession frequencies can be summarized as

$$\omega_{\mathrm{Xe}} = \omega_{d_{\mathrm{Xe}}} + \gamma'_{\mathrm{Xe}}(1-\delta_{\mathrm{Xe}})\langle B\rangle_{\mathrm{Xe}} + \omega^{sd}_{\mathrm{Xe}} + \vec{\Omega}\cdot\hat{B} \tag{4}$$

$$\omega_{\mathrm{He}} = \omega_{d_{\mathrm{He}}} + \gamma'_{\mathrm{He}}(1-\delta_{\mathrm{He}})\langle B\rangle_{\mathrm{He}} + \omega^{sd}_{\mathrm{He}} + \vec{\Omega}\cdot\hat{B}, \tag{5}$$

where
$\gamma'_{\mathrm{Xe/He}} = \frac{2\mu_{\mathrm{Xe/He}}}{\hbar}\sigma_{\mathrm{Xe/He}}$ are the shielded gyromagnetic ratios of the atoms;
$\mu_{\mathrm{Xe/He}}$ are nuclear magnetic moments;
$\sigma_{\mathrm{Xe/He}}$ are the atomic diamagnetic shielding factors;
$\delta_{\mathrm{Xe/He}}$ are species-dependent chemical shifts which depend on pressure, temperature, surrounding materials, etc.;
$\langle B\rangle_{\mathrm{Xe/He}}$ is the magnetic field averaged over space and time in the presence of second- and higher-order gradients, which are not identically averaged by the two species due to different diffusion constants;
$\omega^{sd}_{\mathrm{Xe/He}}$ is the species dependent shift;
$\vec{\Omega}$ is the Earth's angular velocity, and $\vec{\Omega}\cdot\hat{B}$ is its projection onto $\vec{B}$.
The comagnetometer frequency is defined as the combination

$$\omega_{\mathrm{co}} \equiv \omega_{\mathrm{Xe}} - R\omega_{\mathrm{He}}, \tag{6}$$

where $R = 1/2.7540816$ is the nominal ratio of shielded gyromagnetic ratios. Using Eqs. 4 and 5, with $\omega_d \equiv \omega_{d_{\mathrm{Xe}}} - R\omega_{d_{\mathrm{He}}}$, the comagnetometer frequency is

$$\omega_{\mathrm{co}} = \omega_d + \left[\gamma'_{\mathrm{Xe}}(1-\delta_{\mathrm{Xe}})\langle B\rangle_{\mathrm{Xe}} - R\gamma'_{\mathrm{He}}(1-\delta_{\mathrm{He}})\langle B\rangle_{\mathrm{He}}\right] + (\omega^{sd}_{\mathrm{Xe}} - R\omega^{sd}_{\mathrm{He}}) + (1-R)\vec{\Omega}\cdot\hat{B}. \tag{7}$$

Further insight is gained by considering the lowest-order response to changes of $\langle B\rangle_{\mathrm{Xe/He}}$ and $\delta_{\mathrm{Xe/He}}$:

$$\langle B\rangle_{\mathrm{Xe/He}} = B + \Delta B^{\mathrm{dif}}_{\mathrm{Xe/He}},$$

where B is the magnetic field spatially averaged over the cell and $\Delta B^{\mathrm{dif}}_{\mathrm{Xe/He}}$ is the difference of the field actually averaged by the two species.

$$R = R^0 + \Delta R = \frac{\gamma'_{\mathrm{Xe}}(1-\delta_{\mathrm{Xe}})}{\gamma'_{\mathrm{He}}(1-\delta_{\mathrm{He}})},$$

where

$$R^0 = \frac{\gamma'_{\mathrm{Xe}}}{\gamma'_{\mathrm{He}}}; \qquad \Delta R \approx R^0\left(\delta_{\mathrm{He}} - \delta_{\mathrm{Xe}}\right). \tag{8}$$

Therefore, Eq. 7 reduces to

$$\begin{aligned}\omega_{\mathrm{co}} \approx\ & \omega_d \\ & + (1-R)\,\vec{\Omega}\cdot\hat{B} \\ & - \gamma'_{\mathrm{He}}\Delta R B \\ & + \gamma'_{\mathrm{Xe}}\left(\Delta B^{\mathrm{dif}}_{\mathrm{Xe}} - \Delta B^{\mathrm{dif}}_{\mathrm{He}}\right) \\ & + \left(\omega^{sd}_{\mathrm{Xe}} - R\omega^{sd}_{\mathrm{He}}\right).\end{aligned} \tag{9}$$

The 2$^{\mathrm{nd}}$ through 4$^{\mathrm{th}}$ terms in Eq. 9 indicate the sensitivity of ω_{co} to the magnitude, direction, and gradients of the magnetic field. Any correlation of these with the HV may cause a false-EDM signal. Such correlations are expected from possible leakage currents that flow across the cell, magnetization induced by charging currents that flow when the HV is changed, and motion of the measurement cell due to electrostatic forces that change with the HV. Our approach to estimating false-EDM signals is based on auxiliary measurements that measure the comagnetometer frequency response to amplified leakage and charging currents, gradients, and cell motion, which are scaled to the observed maximum of these parameters monitored during the experiment. In Table I, we show how the systematic error from false-EDM effects were determined from auxiliary measurements. The comagnetometer drift is not a direct coupling to the magnetic field and is addressed in the next section.

		Leakage current	Charging current	Cell rotation	Cell translation	
					Linear Gradient	External Dipole (Loop Test)
Auxiliary measurement		Single turn ± 0.1–1 μA	± 10–20 μA	$\pm 5^\circ$	N/A	Loop attached to electrode 0–100 μA
Measured linear dependence		$\frac{1}{2\pi}\frac{\partial\omega_{\rm co}}{\partial I}$	$\frac{1}{2\pi}\frac{\partial\omega_{\rm co}}{\partial I}$	$\frac{1}{2\pi}\frac{\partial\omega_{\rm co}}{\partial\theta}$	$\frac{1}{2\pi}\frac{\partial\omega_{\rm co}}{\partial z}$	$\frac{1}{2\pi}\frac{\partial\omega_{\rm co}}{\partial\omega_{\rm He}}$
	2017	$= (1.32 \pm 0.93)$ Hz/A	$= (-0.3 \pm 1.2)$ mHz/A	≤ 1.6 μHz/rad	≤ 90 nHz/m	$= (-1.55 \pm 0.28) \times 10^{-3}$
	2018	$= (-8.6 \pm 7.6)$ mHz/A			≤ 100 nHz/m	
Observed HV-correlated maximum	2017	$I_{\rm leak} = 97$ pA	$I_{\rm charge} = 19$ nA	$\delta\theta \leq 33$ μrad	$\delta z \leq 200$ μm	$\frac{\delta\omega_{\rm He}^{HV}}{2\pi} = (-181.4 \pm 124.4)$ nHz
	2018	$I_{\rm leak} = 73$ pA	$I_{\rm charge} = 19$ nA			$\frac{\delta\omega_{\rm He}^{HV}}{2\pi} = (-82.5 \pm 226.8)$ nHz
False EDM (e cm)	2017	1.2×10^{-28}	1.7×10^{-29}	4.2×10^{-29}	1.3×10^{-29}	2.6×10^{-28}
	2018	4.5×10^{-31}	1.2×10^{-29}	4.0×10^{-29}	1.0×10^{-29}	1.9×10^{-28}

TABLE I. Systematic effects arising from HV-correlated magnetic field perturbations that lead to false-EDM signals. Each column corresponds to an HV-correlated effect. The HV-correlated frequency shift is found from the linear dependence multiplied by the maximum observed change during the EDM measurements. The false EDM is the 68% CL upper limit of the frequency shift multiplied by the conversion factor 7×10^{-28} e cm/nHz for 2017 and 5×10^{-28} e cm/nHz for 2018. The loop test measured $\frac{\partial\omega_{\rm co}}{\partial\omega_{\rm He}}$ and is most sensitive to the higher-order gradient contribution $\gamma'_{\rm Xe}\left(\Delta B^{\rm dif}_{\rm Xe} - \Delta B^{\rm dif}_{\rm He}\right)$. In lieu of a direct auxiliary measurement of cell translation, this was used to set an upper limit on the false EDM due to cell translation with respect to a gradient source external to the cell, and the total cell translation false EDM added this to the limit on translation coupled to the B dependence. The latter was determined using a measurement of the HV-correlated change in z using a laser beam reflected off the HV electrode to set an upper limit of $\delta z < 200$ μm.

COMAGNETOMETER DRIFT CORRECTION

Uncompensated drift of $\omega_{\rm co}$ would appear as a false EDM due to the frequency shift between segments with opposite $\vec{E} \cdot \hat{B}$. Figs. 2 and 3 show the segment frequencies $\omega_{\rm co}$ as a function of time for a run, illustrating the typical comagnetometer drift of a few μHz over the course of the run. Segment lengths were set guided by the Allan standard deviation such that the segment-to-segment comagnetometer frequency drift was comparable to or less than the statistical error for the segments. These drifts are predominantly due to effects of residual longitudinal magnetization, and recent studies have shown that these drifts are dominated by the combination of two effects: a phase shift induced by the cell-shape dependent torque on the longitudinal magnetization of one species due to the precessing magnetization of the same species [4] and the additional effective static magnetic field exerted on one species due to contact interactions during collisions with the other [4, 5]. The drifts are expected to be a combination of exponential decays due to the T_1 decay of longitudinal magnetization of the two species, assumed to be 5,000–10,000 seconds.

The drifts for all runs were accurately parametrized by polynomials of up to $4^{\rm th}$ order for 2017 and $5^{\rm th}$ order for 2018. The HV reversal pattern shown in Table II was designed to cancel drifts characterized by polynomials of order n for sequences of $N = 2^{n+1}$ segment. For example, a sequence of time-dependent frequencies plus ω_d for equal length segments can be described by

$$\omega_{\rm co}(t_i) = \omega_d + k_0 + k_1 t_i + k_2 t_i^2 + k_3 t_i^3 + \dots, \tag{10}$$

where $t_i = i\Delta t$. The average of $N \geq 1$ consecutive frequencies starting at segment i_0, with $i_0 = 1, 1+N, 1+2N, \dots$, is

$$\bar{\omega}_d = \frac{1}{N}\sum_{i=i_0}^{i_0+N} S_i^{EB}\omega_{\rm co} = -\frac{2d|E|}{\hbar} + c_1 k_1 \Delta t + c_2 k_2 \Delta t^2 + \dots + c_n k_n \Delta t^n, \tag{11}$$

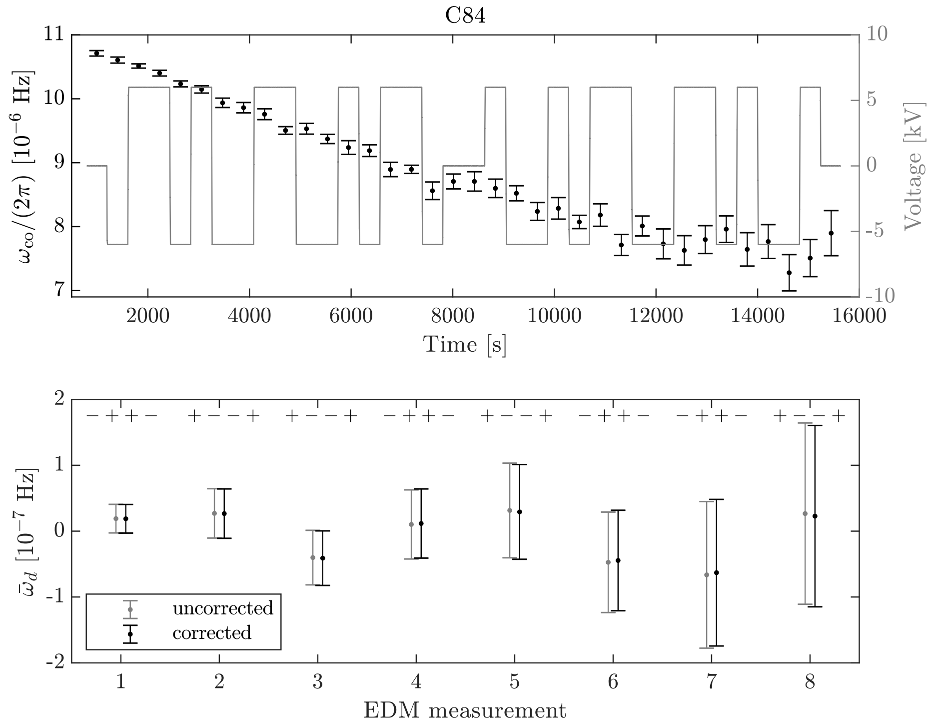

FIG. 2. Top: Segment frequencies $\omega_{\rm co}$ (left axis) and the HV pattern (right axis) for run C84 in 2017. The offset of the comagnetometer frequency is due largely to the combination of the chemical shift and Earth's rotation, which are compensated by combining segment frequencies in combinations of two or more segments with opposite HV. See Eq. 9 and the following discussion. Bottom: Four-segment EDMs, which compensate linear drifts; (left/gray) uncorrected and (right/black) corrected for higher order drifts. While corrections for each 4-segment EDM are illustrated here, in the analysis the correction was applied per subrun. As shown in Table II, the drift correction reverses with the polarity of the first HV segment in the sequence of four and increases in magnitude later in the run.

where $S_i^{EB} = \mathrm{sgn}(\hat{E}\cdot\hat{B})$ and

$$c_1 = \frac{1}{N}\sum_{i=i_0}^{i_0+N} S_i^{EB} i = \frac{1}{N}\left[i_0 - (i_0+1) - (i_0-2) + (i_0+3) + \dots\right],$$

$$c_2 = \frac{1}{N}\sum_{i=i_0}^{i_0+N} S_i^{EB} i^2, \qquad \text{etc.} \tag{12}$$

For $N = 4$, $c_1 = 0$, for $N = 8$, $c_2 = c_1 = 0$, *etc.*. The values of c_{2-4} for the four-segment sequence ($N = 4$) are given in Table II. Because the signals decay, the frequency uncertainty per segment increases over time. Since the combination of N segments for an EDM measurement is an unweighted average, using larger N sequences result in larger statistical error in the final weighted average of EDM measurements. Because the observed drifts were mostly linear, a $N = 4$ sequence was used in the analysis and the correction for higher-order drifts was small compared to the statistical error.

For each run, the comagnetometer frequencies were fit to second, third and fourth order polynomials in 2017 and up to fifth order in 2018, and the F-test statistic was calculated for each increasing polynomial order. Table III shows the integrated probability $\int_{F_{\rm min}}^{\infty} P(F)dF$ for adding a quadratic, cubic, and quartic term for all runs in 2017. For each run, a correction was applied to $\bar{\omega}_d$ for each polynomial order if the integrated probability exceeded a specific threshold. The threshold of 0.6 was chosen by using blinded frequencies based on the range over which the uncertainty of the correction was relatively constant. Since the blind for 2017 was applied as a frequency, the EDM was offset by different amounts for the two cells and the final correction was therefore determined from the difference of corrected and uncorrected unblinded EDMs, which are shown as a function of threshold for 2017 in Table IV. The bottom panel of Fig. 2 shows $\bar{\omega}_d$ for a single run along with the corrections for higher order drift. The corrections alternate with the HV polarity at the start of the four-segment sequence, but do not fully cancel for a run. For a threshold of 0.6,

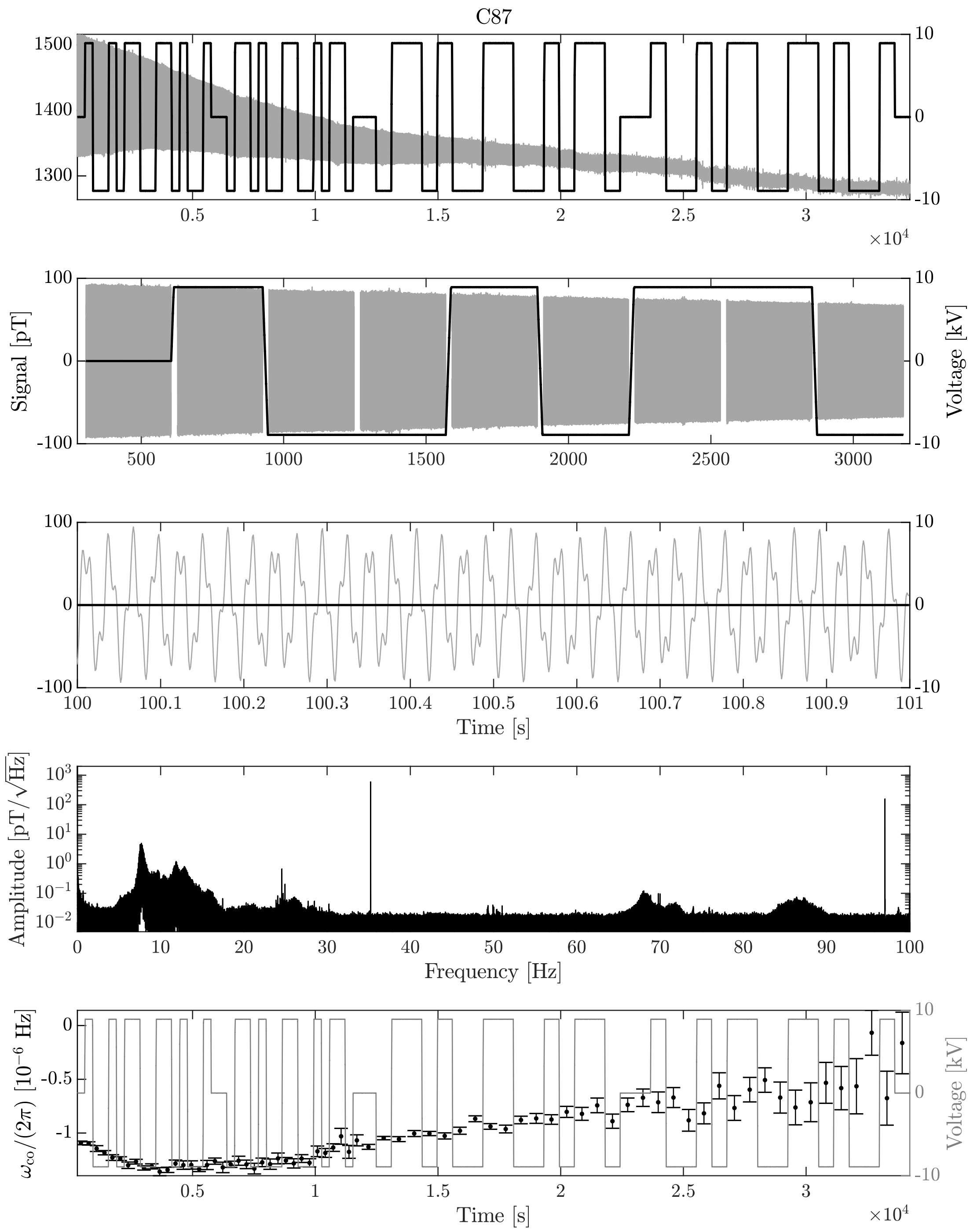

FIG. 3. Top: Unfiltered data (left axis, gray) and the HV pattern (right axis, black) for a run in 2018 with two subruns. Second from top: High-pass filtered data (left axis, gray) that has been cut according to the HV states (right axis, gray). Middle: One second of high-pass filtered data shows the two frequencies (35 Hz for ^{129}Xe and 90 Hz for ^{3}He) superposed. Fourth from top: FFT of unfiltered signal. Bottom: Segment frequencies ω_{co} (left axis) and the HV pattern (right axis).

Segment	S^{EB}	c_2	c_3	c_4	Segment	S^{EB}	c_2	c_3	c_4
0	0				18	0			
1	+	1	7.5	40	19	−	−1	−61.5	−2524
2	−				20	+			
3	−				21	+			
4	+				22	−			
5	−	−1	−19.5	−256	23	+	1	73.5	3604
6	+				24	−			
7	+				25	−			
8	−				26	+			
9	−	−1	−31.5	−664	27	+	1	85.5	4876
10	+				28	−			
11	+				29	−			
12	−				30	+			
13	+	1	43.5	1264	31	−	−1	−97.5	−6340
14	−				32	+			
15	−				33	+			
16	+				34	−			
17	0				35	0			

TABLE II. HV pattern and weights c_i for polynomial fit coefficients k_i used in higher-order drift corrections for 18 and 36 segments of a run starting with +HV. For runs starting with −HV, the patterns and coefficients are reversed (multiply by −1).

the correction was $(-0.08 \pm 0.66) \times 10^{-27}$ $e\,$cm, where the uncertainty is a statistical error based on the polynomial fits to the segment frequencies for each run.

CORRELATIONS

The consistency of the EDM measurements was checked under different conditions including gas pressure, measurement cell, HV ramp rate, HV segment length, and HV polarity at the start of a subrun, and $\hat{\mathbf{B}}_\mathbf{0}$ for 2017 and 2018 (See Fig. 4). Each of these couples to the systematic effects discussed previously. Varying gas pressure couples to the second and fourth term of Eq. 7 because of differences in the chemical shift and averaging of magnetic gradients within the cell. The measurement cells used have different dimensions and therefore both the size and time dependence (from different T_1) of the comagnetometer drift may change. For different HV ramp rates, the charging current changes. Correlations with HV segment length and HV polarity may indicate a systematic error from the comagnetometer drift correction. $\hat{B}_0$ couples to the earth's rotation and to the gradients from any nearby stationary dipole. Figs. 5 and 6 show fits of the EDM versus experimental parameters including pressure, segment length, T_2^* and the linear and quadratic polynomial fit coefficients for 2017 and 2018, respectively.

* sachd@umich.edu

[1] G. Golub and V. Pereyra, Inverse Problems **19**, R1 (2003).
[2] I. Fan *et al.*, Journal of Physics: Conference Series **723**, 012045 (2016).
[3] V. V. Flambaum and J. S. M. Ginges, Phys. Rev. A **65**, 032113 (2002).
[4] W. A. Terrano, J. Meinel, N. Sachdeva, T. E. Chupp, S. Degenkolb, P. Fierlinger, F. Kuchler, and J. T. Singh, Phys. Rev. A **100**, 012502 (2019).
[5] M. E. Limes, N. Dural, M. V. Romalis, E. L. Foley, T. W. Kornack, A. Nelson, L. R. Grisham, and J. Vaara, Phys. Rev. A **100**, 010501 (2019).

Run	Cell	Quadratic	Cubic	Quartic
C82	PP2	1.00	0.86	0.82
C83	PP2	0.98	0.85	0.08
C84	PP2	1.00	0.98	0.45
C85	PP2	0.90	0.48	0.14
C86	PP1	0.98	0.89	0.86
C89	PP1	0.14	0.57	0.47
C91	PP1	1.00	0.34	0.65
C92	PP1	1.00	0.73	0.70
C93	PP2	1.00	0.64	0.07
C02	PP2	1.00	0.04	0.94
C08	PP2	0.99	1.00	0.01
C10	PP1	1.00	0.89	0.86
C12	PP2	0.99	0.37	0.08
C13	PP2	0.25	1.00	0.40
C14	PP2	1.00	0.72	0.52
C15	PP1	0.99	0.85	0.78

TABLE III. $\int_{F_{\min}}^{\infty} P(F)dF$ by run in 2017 for quadratic, cubic, and quartic terms in the polynomial fit. For C13, quadratic and cubic terms were included for the drift correction.

$P_{\text{thres.}}$	d_{cor} $(10^{-27}\ e\,\text{cm})$	$\sigma_{d_{\text{cor}}}$ $(10^{-27}\ e\,\text{cm})$	correction $(10^{-27}\ e\,\text{cm})$	σ_{cor} $(10^{-27}\ e\,\text{cm})$
0	−0.42	2.59	−0.76	1.13
0.2	−0.29	2.55	−0.63	1.04
0.4	0.20	2.43	−0.14	0.69
0.5	0.21	2.43	−0.13	0.69
0.6	0.26	2.42	−0.08	0.66
0.8	0.24	2.36	−0.10	0.36
no correction	0.34	2.33	N/A	N/A

TABLE IV. Results for the corrected EDM in 2017 as a function of the threshold for $\int_{F_{\min}}^{\infty} P(F)dF > P_{\text{thres.}}$. The correction is the difference between the corrected EDM d_{cor} and the uncorrected EDM d_{uncor}, and the uncertainty of the correction σ_{cor} is estimated such that $\sigma_{d_{\text{cor}}} = \sqrt{\sigma^2_{d_{\text{uncor}}} + \sigma^2_{\text{cor}}}$. For both 2017 and 2018, a threshold of $P_{\text{thres.}} = 0.6$ was used.

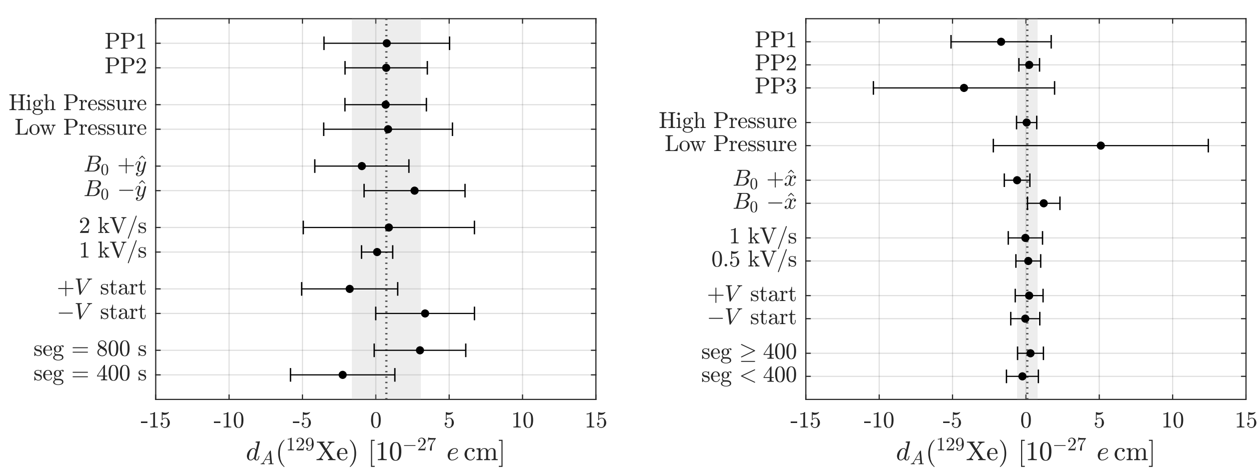

FIG. 4. Correlations with various experimental parameters for 2017 (left) and 2018 (right). The dotted line is the weighted average of all subruns for each campaign and the shaded region is 1 σ.

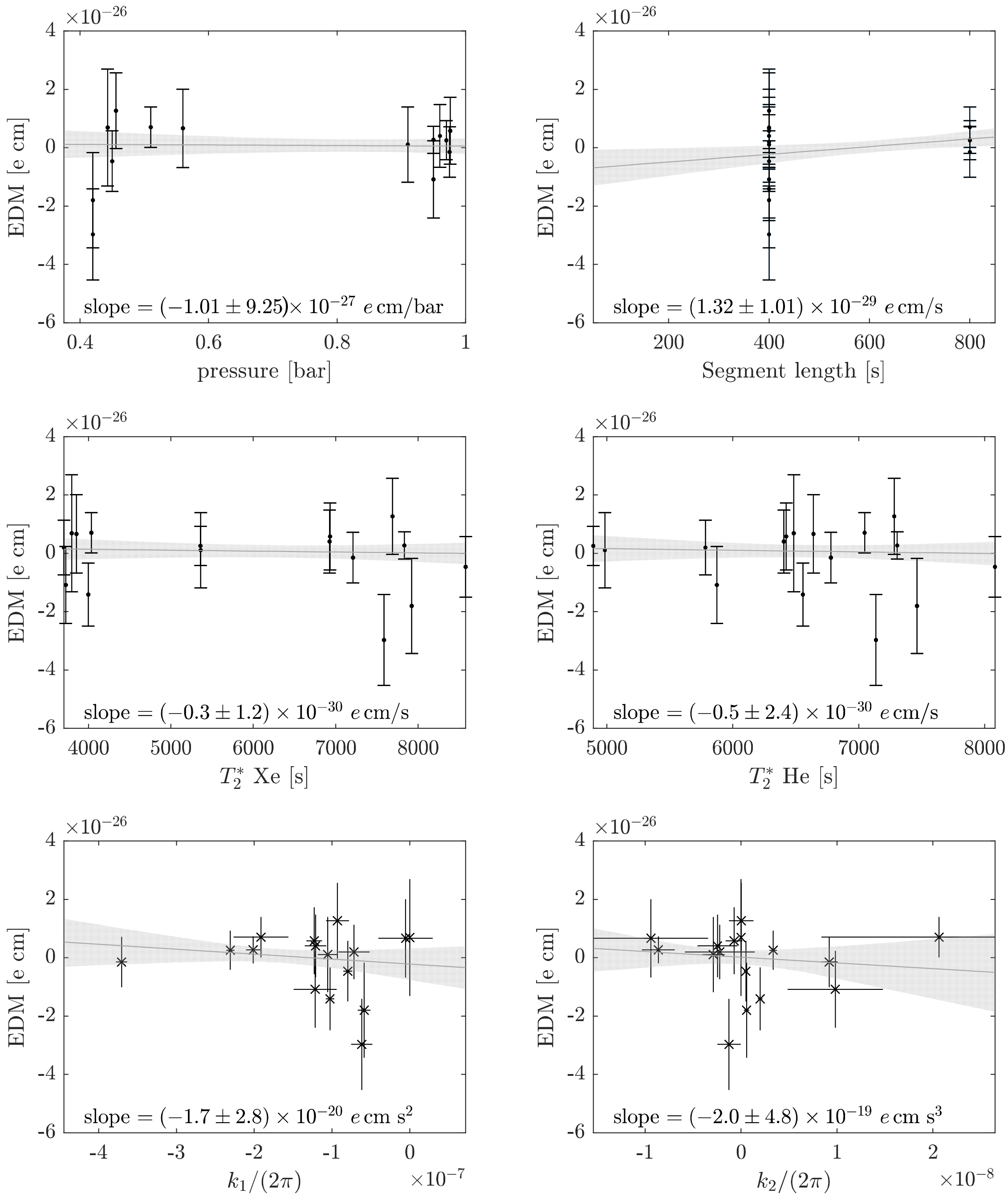

FIG. 5. Correlations with pressure, segment length, T_2^* and the linear and quadratic fit coefficients from the polynomial fits per run in 2017.

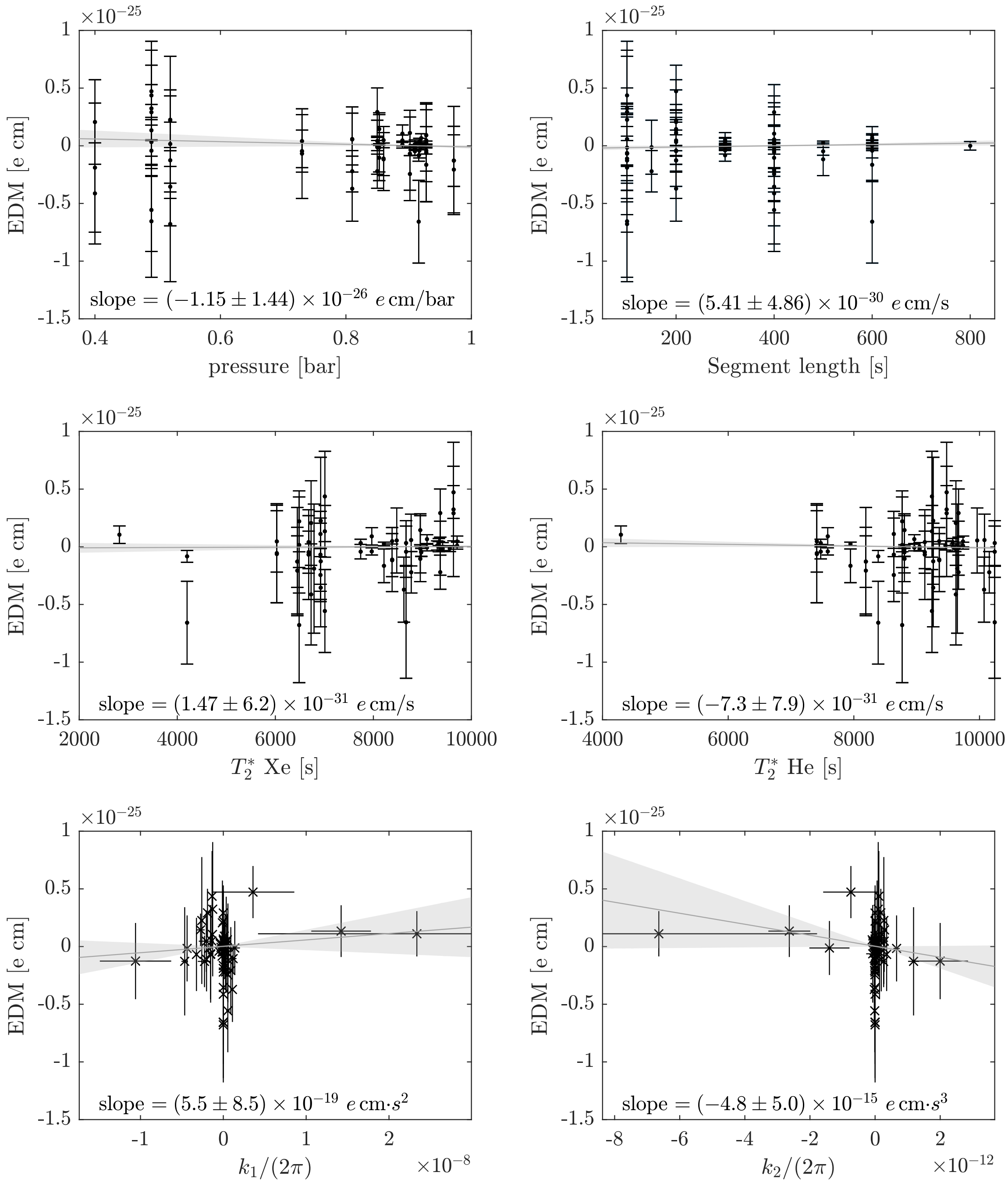

FIG. 6. Correlations with pressure, segment length, T_2^* and the linear and quadratic fit coefficients from the polynomial fits per subrun in 2018.